Chinese Chemical Letters 36 (2025) 110133

Contents lists available at ScienceDirect

Chinese Chemical Letters

journal homepage: www.elsevier.com/locate/cclet

Biomimetic nanofibrillar/hyaluronic acid hydrogels remodel the neuromodulatory microenvironment for enhanced bone regeneration

Jielin Wang[a,b,c,1,*], Han Ye[d,1], Bozhuang Zhou[e], Zhen Pan[f], Yucai Li[f], Zhenyuan Wei[f], Bin Chai[f], Yizhou Gao[e,*], Xiaojian Ye[a,b,c,f,*], Jiangming Yu[a,b,f,*]

[a] Laboratory of Key Technology and Materials in Minimally Invasive Spine Surgery, Tongren Hospital, Shanghai Jiao Tong University School of Medicine, Shanghai 200336, China
[b] Shanghai Jiao Tong University Spinal Minimally Invasive Research Center, Tongren Hospital, Shanghai Jiao Tong University School of Medicine, Shanghai 200336, China
[c] Hongqiao International Institute of Medicine, Tongren Hospital, Shanghai Jiao Tong University School of Medicine, Shanghai 200336, China
[d] Department of Ophthalmology and Vision Science, Shanghai Eye Ear Nose and Throat Hospital, Fudan University, Shanghai 200126, China
[e] The Center for Microbes Development and Health, Shanghai Insititute of Immunity and Infection Chineses Academy of Science, Shanghai 200031, China
[f] Department of Orthopaedic, Tongren Hospital, Shanghai Jiao Tong University School of Medicine, Shanghai 200336, China

ARTICLE INFO

Article history:
Received 2 April 2024
Revised 13 June 2024
Accepted 17 June 2024
Available online 17 June 2024

Keywords:
Neuroregulation
Vasoactive intestinal peptide
Nerve growth factor
Biomimetic extracellular matrix
Bone regeneration

ABSTRACT

Severe traumatic bone healing relies on the involvement of growth factors. However, excessive supplementation of growth factors can lead to ectopic ossification and inflammation. In this study, utilizing the neural regulatory mechanism of bone regeneration, we have developed a multifunctional three dimensions (3D) printed scaffold containing both vasoactive intestinal peptide (VIP) and nerve growth factor (NGF) as an effective new method for achieving bone defect regeneration. The scaffold is provided by a controlled biodegradable and biomechanically matched poly(lactide-ethylene glycol-trimethylene carbonate) (PLTG), providing long-term support for the bone healing cycle. Factor loading is provided by peptide fiber-reinforced biomimetic antimicrobial extracellular matrix (ECM) (B-ECM) hydrogels with different release kinetics, the hydrogel guides rapid bone growth and resists bacterial infection at the early stage of healing. Physical and chemical characterization indicates that the scaffold has good structural stability and mechanical properties, providing an ideal 3D microenvironment for bone reconstruction. In the skull defect model, compared to releasing VIP or NGF alone, this drug delivery system can simulate a natural healing cascade of controllable release factors, significantly accelerating nerve/vascular bone regeneration. In conclusion, this study provides a promising strategy for implanting materials to repair bone defects by utilizing neuroregulatory mechanisms during bone regeneration.

The treatment of large segment bone defects has always been a focus of attention for clinicians [1-3]. The emergence and in-depth research of bone tissue engineering have brought the dawn of bone repair [4,5]. However, natural bone tissue has a unique structure and tissue distribution, it is difficult for traditional scaffold preparation technology to imitate the complex structure of functional tissues and achieve the precise localization of multiple cells in scaffolds [6,7]. Therefore, it remains a major challenge to construct scaffolds similar to natural bone tissue from the perspective of structure and function [8-10]. In recent years, three dimensions (3D) bioprinting technology has been widely studied in bone tissue applications due to its accuracy and repeatability in preparing scaffolds [11,12].

In our preliminary study, a ternary copolymer poly(lactide-glycolide-trimethylene carbonate) (PLGT) was synthesized by copolymerization modification of poly-L-lactic acid (PLLA) for bone stents, and it have proved that terpolymer has excellent effect in repairing large segment bone defects [13-15]. In this study, we redesigned and modified PLGT polymer based on the mechanical and degradation properties required for bone defect repair, and innovated the raw materials used for 3D printing. By utilizing the good flexibility of the poly-trimethylene carbonate (PTMC) segment, the toughness of the PLLA main chain can be improved. By increasing the content of glycolide (GA) units in the main chain, the overall strength of the random block copolymer can be controlled, and the degradation rate of PLLA can be accelerated. The designed and synthesized copolymer of PLGT can not only guarantee the strength

* Corresponding authors.
E-mail addresses: wangjielin369@126.com (J. Wang), gaoyizhou@126.com (Y. Gao), yexj2002@163.com (X. Ye), yjm_st@163.com (J. Yu).
[1] These authors contributed equally to this work.

https://doi.org/10.1016/j.cclet.2024.110133
1001-8417/

and toughness of polyester material but also improve the characteristics of slow degradation of polyester, which is in line with the requirements of mechanics and biodegradable activity. But its surface lacks activity, which is not conducive to early cell adhesion and osteogenic induction, so it needs to be surface modified.

In recent years, more and more evidence has supported the role of the nervous system in bone regeneration, the peripheral nerves within the skeleton generate a large amount of signals through the secretion of neurotransmitters, neuropeptides, axon guiding factors, and neurotrophic factors, which participate in bone development and repair [16-20]. Therefore, by utilizing the connection between bones and nerves, tissue engineering scaffolds can be designed for repairing bone defects. Vasoactive intestinal peptide (VIP) [21,22] is expressed and secreted by sympathetic nerve fibers, studies have reported that VIP has a significant proliferative effect on human umbilical vein endothelial cells (HUVECs), and can significantly enhance the synthesis of vascular endothelial growth factor (VEGF) in HUVECs. VIP, as the first messenger, activates G protein by binding to specific receptors on the HUVECs membrane, leading to an increase in intracellular adenylate cyclase (AC) activity, simultaneously reducing intracellular glucocorticoid (GC) activity leads to an increase in intracellular adenosine monophosphate (cAMP) concentration and a decrease in cyclic guanosine monophosphate (cGMP) concentration, and activate the inositol triphosphate (IP3) system to reduce and increase intracellular [Ca^{2+}] levels through the release of intracellular Ca^{2+} and changes in ion channel opening on the cell membrane, thereby enhancing VEGF expression. Neurotrophic factors are factors that can support neural activity, such as axon growth, synaptic plasticity, cell survival, differentiation, and myelin formation [23]. Among them, nerve growth factor (NGF) can affect bone reconstruction by regulating osteogenesis and bone resorption. NGF receptors are expressed on the surface of osteoblasts, osteoclasts, and chondrocytes. During the early stages of bone repair, NGF expression is significantly upregulated, while in the later stage of bone healing, the activity of NGF is significantly reduced [24,25]. Studies have shown that NGF can prevent osteoblast apoptosis and induce osteoblast differentiation, and blocking the expression of NGF in sensory nerve is not conducive to the ossification process of long bone [26].

Hydrogels are widely used as cell culture scaffolds for tissue formation and regeneration [27,28], and are also one of the means to deliver growth factors to promote repair [29-33]. The interpenetrating polymer network (IPN) hydrogel scaffold with independent and functional networks can simulate various natural extracellular matrix (ECM) environments. Studies have proved that the most characteristic interpenetrating network structure of peptide fiber reinforced hydrogel can conveniently load different growth factors, and the controllable release is more accurate, which is more conducive to cell culture than simple hydrogels [34-36]. Based on this, we designed a new peptide fiber reinforced hydrogel two factor release system in this study, The system consists of Ac-$(KAEA)_4$-NH_2 (KA) peptides that can self-assemble into nanofibers, Ac-$(KAEA)_4$GPRGDSGRGDS-NH_2 (KS) peptides with cell adhesion, and Ac-$(KAEA)_4$GYGLFRIIKKIARSF-NH_2 (KF) peptides with antibacterial properties [37], VIP is loaded into peptide fibers by physical blending. The hydrogel portion consists of maleaminated polyethylene glycol (PEG) (MAL-PEG-MAL) cross-linked mercaptohyaluronic acid (HA-SH), NGF was chemically grafted into the hydrogel by crosslinking agent. Because the peptide fiber reinforced hydrogel also has the characteristics of simulating the structure of natural ECM, it is named B-ECM.

In this study, we designed a novel biodegradable PLLA-GA-TMC (PLGT) ternary random block copolymer as the ink, and constructed a porous mechanical support scaffold through 3D printing; the composite scaffold filled with a difactor B-ECM hydrogel

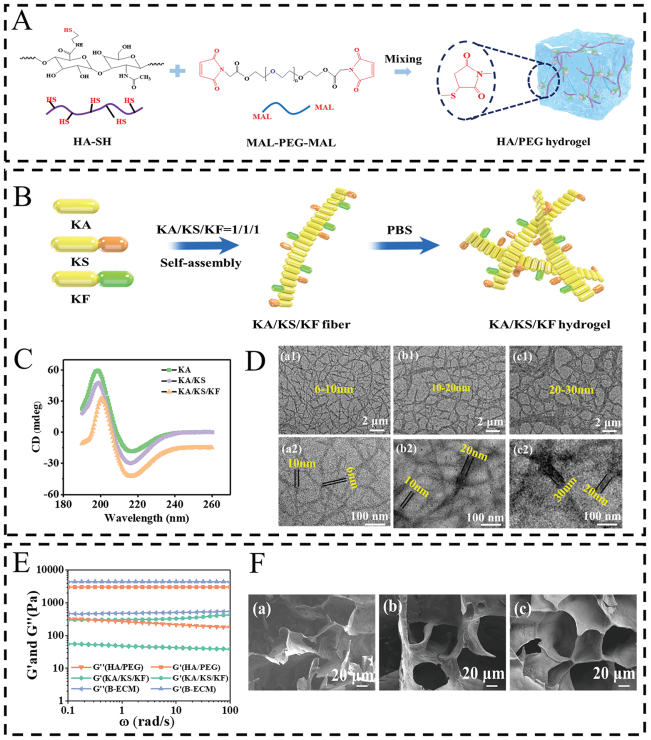

Fig. 1. Characterization of the B-ECM hydrogel. (A) Schematic illustration for the fabrication of HA/PEG hydrogel. (B) Schematic illustration for the self-assembly KA/KS/KF functional polypeptide. (C) Circular dichroism of KA, KA/KS and KA/KS/KF. (D) TEM photographs of KA (a1, a2), KA/KS (b1, b2) and KA/KS/KF (c1, c2). (E) Rheological scanning diagram of pure HA/PEG, KA/KS/KF and B-ECM hydrogel. (F) SEM images of the cross-section morphology of hydrogels. (a) HA/PEG, (b) KA/KS/KF and (c) B-ECM.

KA/KS/KF@VIP/HA-PEG@NGF (B-ECM@VN), provide precise content control and sequential delivery of VIP and NGF, to improve biocompatibility and bone inducibility, simultaneously possessing antibacterial properties.

Performance analysis of 3D printed PLGT polyester materials can be found in Fig. S1 (Supporting information). The cross-linking principle of HA/PEG is shown in Fig. 1A. Since it is easy to form stable thioether bond between maleimide and mercapto at pH 6.5–7.5, this study adopted maleimide PEG (MAL-PEG-MAL) crosslinking sulfhydrylated HA (HA-SH) to form HA/PEG hydrogel. Fig. S2 (Supporting information) shows the infrared spectra of HA-SH, MAL-PEG-MAL and HA/PEG. In the HA-SH spectrum, 2513 cm^{-1} is the stretching vibration peak of -SH, indicating that the new substance has a -SH group. It can be seen from MAL-PEG-MAL spectrum that after the modification of maleimide at both ends of the PEG terminal group, the hydroxyl absorption peak of PEG at about 3300 cm^{-1} disappears, while the new peak appearing at about 1709 cm^{-1} belongs to the carbonyl absorption peak of maleimide, thus the successful synthesis of maleimide polyethylene glycol can be obtained. It can be seen from the HA/PEG spectrum that after the reaction between HA-SH and MAL-PEG-MAL, not only the typical absorption peaks of the two substances appear in the infrared spectrum, but also the mercaptoyl peaks in HA-SH disappear, indicating that HA-SH has a bonding reaction with MAL-PEG-MAL. The presence of the characteristic proton peak in the ^1H NMR (Fig. S3 in Supporting information) also proves that the sulfydryl group has a michael addition reaction with maleimide. At room temperature, after mixing the HA-SH solution with MAL-PEG-MAL crosslinker solution, a vial tilt test was carried out. As shown in Fig. S4 (Supporting information), when the concentration of HA-SH was less than 5.0 wt%, the addition of MAL-PEG-MAL cross-linking

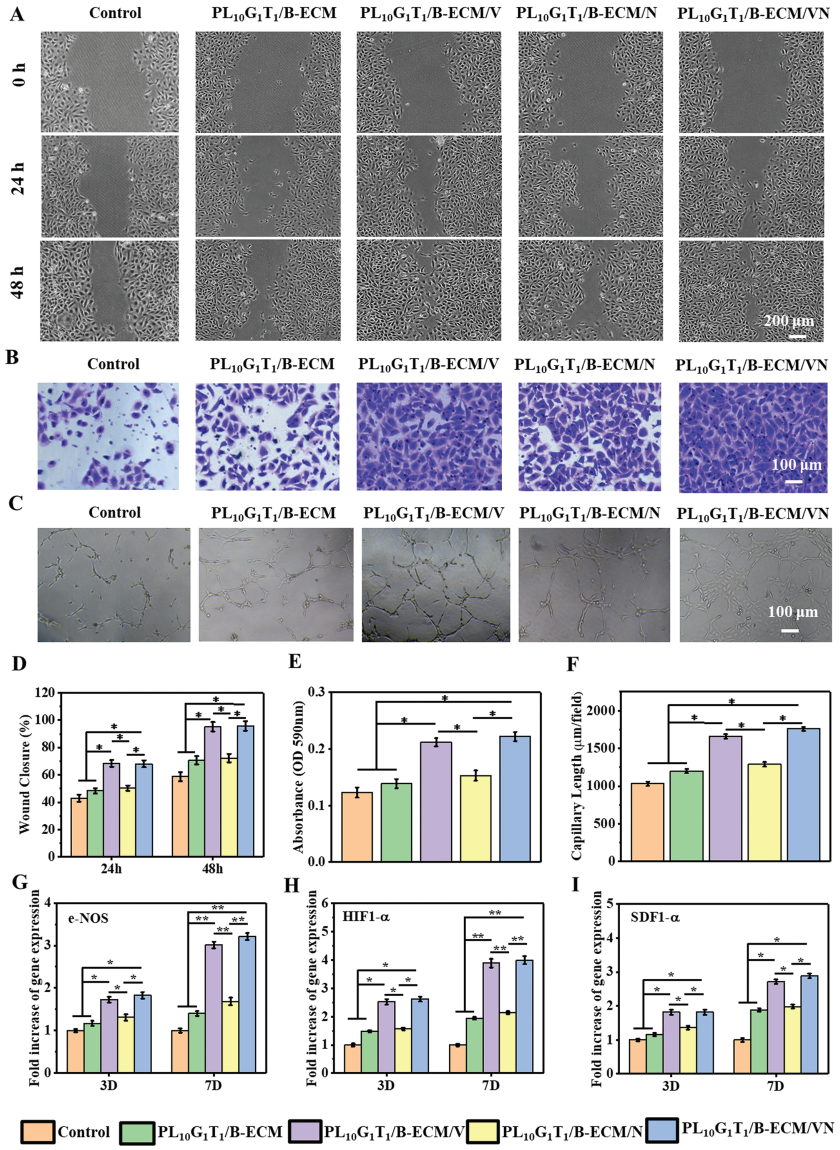

Fig. 2. Effects of different scaffolds extract on HUVECs migration, tubular network formation and angiogenesis genes expression. (A) Representative images of scratch wound healing assay at 0, 24 and 48 h. (B) Representative images of the transwell migration assay at 24 h. (C) The tubular network formation of HUVECs after 9 h incubation. (D) Quantitative analysis of scratch healing rate by the microscopic photographs. (E) Quantitative analysis of HUVECS migration by the OD value of crystal violet. (F) Quantitatively analyzed capillary length by ImageJ software. (G–I) Effect of the different scaffolds extract on the angiogenesis genes expression in HUVECs at 3 and 7 days by qRT-PCR analysis including (G) e-NOS, (H) HIF1-α and (I) SDF1-α. The control group HUVECs were cultured with a normal medium. Data are presented as mean ± standard deviation (SD) ($n = 3$). $^{*}P < 0.05$, $^{**}P < 0.01$.

agent could not form gel. When the concentration of HA/PEG was 5.0/3.0 wt%, hydrogel could be formed within 10 min. The self-assembly diagram of the peptide is shown in Fig. 1B. In the circular two-dimensional chromatogram (Fig. 1C), KA, functional self-assembled peptide mixed solution KA/KS and KA/KS/KF all exhibit typical β-folded structure spectra, with the highest characteristic peak at 195 nm and the lowest characteristic peak at 216 nm [38,39]. It can be observed from transmission electron microscope (TEM) images (Fig. 1D) that the diameter of nanofibers assembled with mixed peptides is larger than that assembled with pure KA peptide. The diameter ranges of KA, KA/KS, and KA/KS/KF peptides are (6–10 nm), (10–20 nm) and (20–30 nm), respectively. The fiber diameters of different peptides are consistent with the number of amino acids in the peptides. Fig. 1E is the rheological scanning diagram of pure HA/PEG, KA/KS/KF and B-ECM hydrogel (concentration 5%/3%/3%). The G' of all hydrogels is greater than G", which confirms the solid phase property (formation of elastic hydrogels) of these hydrogels. Further, it can be seen that the elastic modulus of B-ECM hydrogels is higher than that of pure peptide and pure HA/PEG hydrogels, which is due to the introduction of HA, enhances the hydrogel network crosslinking through macromolecular entanglement and hydrogen bond formation. Fig. 1F shows the SEM images of pure HA/PEG, KA/KS/KF and B-ECM hydrogels after freeze-drying. All hydrogels show porous microstructures with pore sizes ranging from 20 μm to 100 μm. When the double network hydrogel is formed, its porous structure is similar to that of HA/PEG in the same proportion, and the addition of polypeptide does not change the network structure of the hydrogel. All hydrogels are very close to the state of swelling equilibrium after soaking for 10 h (Fig. S5 in Supporting information) and all hydrogel showed good degradability and stability, satisfying the needs of bone regeneration period and facilitating the transfer of growth factors (Fig. S6 in Supporting information).

The new 3D printed $PL_{10}G_1T_1$ scaffold with uniform large holes and the B-ECM hydrogel filled $PL_{10}G_1T_1$ scaffold are shown in Fig. S7 (Supporting information). The fiber diameter and pore size are

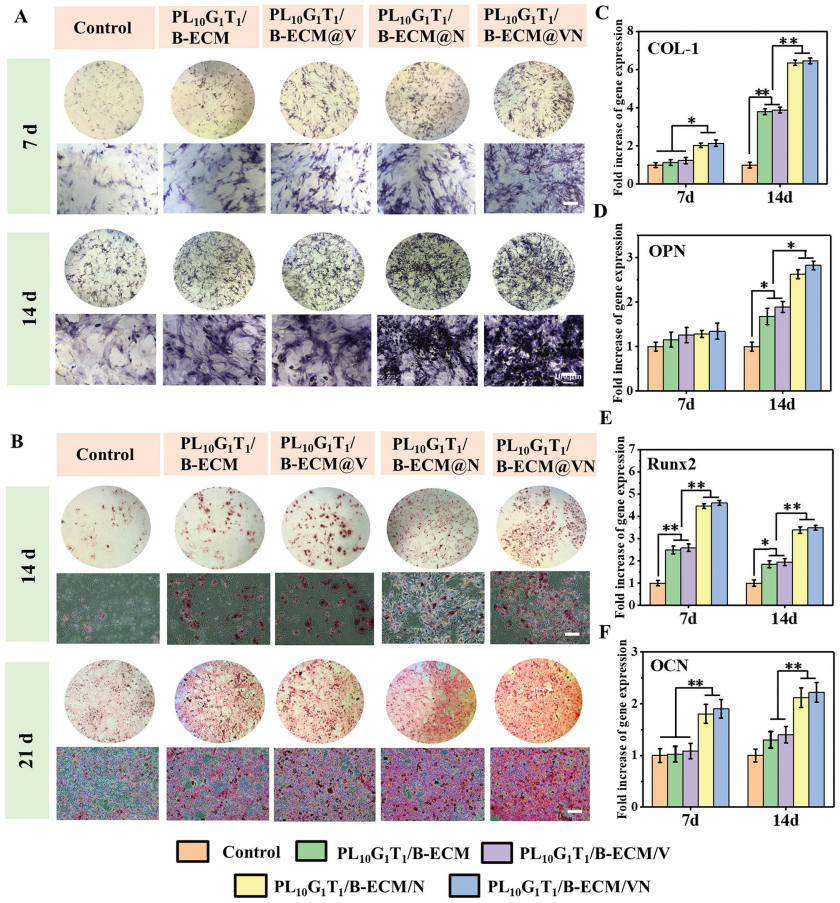

Fig. 3. Evaluation of the osteogenic potential of different scaffolds extract. (A) Digital and microscopic images of ALP staining of rat BMSCs cultured with different scaffolds extract at 7 and 14 days. (B) Digital and microscopic images of Alizarin Red-S staining of rat BMSCs cultured with different scaffolds extract at 14 and 21 days. (C–F) Effect of the different scaffolds extract on the osteogenic genes expression in rat BMSCs at 7 and 14 days by qRT-PCR analysis including (C) COL-1, (D) OPN, (E) Runx2 and (F) OCN. Rat BMSCs were cultured with the conditioned medium. Data are presented as mean ± SD ($n = 3$). $^{*}P < 0.05$, $^{**}P < 0.01$. Scale bar: 200 μm.

0.425 ± 0.013 and 0.392 ± 0.036 mm, respectively (Fig. S7A). The filling of B-ECM hydrogel increased the hydrophilicity of $PL_{10}G_1T_1$ scaffold, and the higher the concentration of B-ECM, the better the hydrophilicity (Fig. S7B). CCK-8 and dead/alive staining experiments indicated that the graded release of VIP helps to promote cell proliferation (Figs. S7C–E). VIP loaded in the polypeptide hydrogel component through physical blending had a rapid release process in the first 8 days, and the release was complete in about 12 days. NGF in the HA/PEG hydrogel component was released slowly by chemical grafting and could be released sustainably for about 30 days (Fig. S7F). In summary, the composite stent achieves controlled graded delivery of VIP and NGF, which may help improve the vascularization rate and efficient osteogenic differentiation at the defect site [40].

To evaluate its neurogenetic capacity, the effect of $PL_{10}G_1T_1$/B-ECM@VN on the neurite elongation of rat dorsal root ganglion cells (DRGs) *in vitro* was evaluated by immunofluorescence. As shown in Fig. S8 (Supporting information), the $PL_{10}G_1T_1$/B-ECM@VN scaffold significantly promoted neurite elongation of DRGs cells, demonstrating its *in vitro* ability to stimulate neurogenesis and thereby enhance neuro-bone crosstalk [41]. The scratch test results were shown in Fig. 2A. Cell migration occurred in all groups, and the control group had the slowest migration effect. After 48 h, the cell migration effect of group $PL_{10}G_1T_1$/B-ECM@V and $PL_{10}G_1T_1$/B-ECM@VN was the most significant, and the scratches were almost closed, followed by the effect of group $PL_{10}G_1T_1$/B-ECM@N and $PL_{10}G_1T_1$/B-ECM. The results of quantitative analysis are shown in Fig. 2D. Group $PL_{10}G_1T_1$/B-ECM@V and $PL_{10}G_1T_1$/B-ECM@VN is best because of the network structure of the hydrogel and the release of VIP. Secondly, the results of Transwell cell experiment (Fig. 2B) and the optical density (OD) value measured by crystal purple (Fig. 2E) once again proved that B-ECM hydrogel loaded with VIP factors could further promote HUVECs migration. Furthermore, the influence of scaffolds on angiogenesis in HUVECs was further detected by Matrigel tube formation experiment. The results of HUVECs cultured on the surface of Matrigel for 9 h were shown in Fig. 2C and the capillary length (Fig. 2F) in each group at 9 h were quantitatively analyzed using ImageJ software. All scaffolds could induce the formation of tubular networks after 9 h. It can be clearly seen that the tubular network formation in groups $PL_{10}G_1T_1$/B-ECM@V and $PL_{10}G_1T_1$/B-ECM@VN is significantly better than that other three groups. The above results indicated that hydrogels were beneficial to inducing migration of HUVECs cells, the $PL_{10}G_1T_1$/B-ECM@V and $PL_{10}G_1T_1$/B-ECM@VN group indicated that scaffolds loaded with VIP accelerated the formation of induced tubular networks and capillary structures. In addition, the effect of VIP release on the angiogenic genes of HUVECs was studied by qPCR (Figs. 2G–I). The expression levels of endothelial nitric oxide synthase (e-NOS), hypoxia inducible factor-1α (HIF1-α) and stromal cell-derived factor-1α (SDF1-α) in HUVECs cultured in group $PL_{10}G_1T_1$/B-ECM@V and $PL_{10}G_1T_1$/B-ECM@VN were significantly higher than those in control group, group $PL_{10}G_1T_1$/B-ECM and group $PL_{10}G_1T_1$/B-ECM@N, which confirmed that VIP was involved in the regulation of HIF1-α signaling pathway.

Alkaline phosphatase (ALP) activity of bone marrow mesenchymal stem cells (BMSCs) was detected and ALP staining was per-

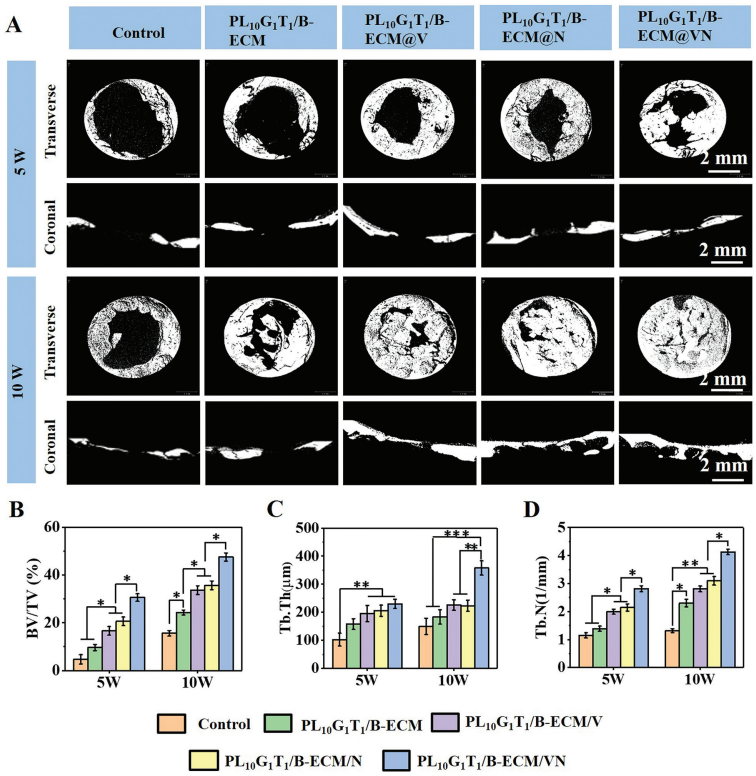

Fig. 4. Bone regeneration at 5 and 10 weeks after implantation of different scaffolds in Sprague-Dawley rat skull defect models. The control group was the skull defect group without scaffold implantation. (A) Representative 3D reconstructed micro computed tomography (Micro-CT) images including transverse and coronal sections. Quantitative analysis of (B) BV/TV, (C) trabecular thickness (Tb.Th) and (D) trabecular number (Tb.N), by Micro-CT. Data are presented as mean ± SD ($n = 3$). $^{*}P < 0.05$, $^{**}P < 0.01$, $^{***}P < 0.001$.

formed to observe the osteogenic differentiation of BMSCS at 7 and 14 days, respectively (Fig. 3A). The results showed that the $PL_{10}G_1T_1$/B-ECM@N and $PL_{10}G_1T_1$/B-ECM@VN group has no difference in ALP activity, but it was significantly higher than other groups on days 7 and 14, and showing a more pronounced degree of ALP staining. The quantitative detection of ALP was shown in Fig. S9 (Supporting information). During the culture time, the ALP activity of cells in each group gradually increased with the extension of time, which was consistent with the ALP staining intensity. Fig. 3B shows the optical and microscope images stained with alizarin red after 14 and 21 days of BMSCs cultured with different scaffold extracts. It can be seen that the color intensity of group $PL_{10}G_1T_1$/B-ECM@N and $PL_{10}G_1T_1$/B-ECM@VN was similar and higher than other groups. The quantitative analysis of alizarin red staining (Fig. S10 in Supporting information) and the calcium content of different extracts (Fig. S11 in Supporting information) are consistent with this result. In conclusion, the results showed that the continuous release of NGF was more conducive to matrix mineralization at the end of osteogenic differentiation of BMSCs. The results of qPCR (Figs. 3C–F) showed that the expressions of collagen type I (COL-1), osteopontin (OPN), runt-related transcription factor 2 (Runx2) and osteocalcin (OCN), in the $PL_{10}G_1T_1$/B-ECM@N and $PL_{10}G_1T_1$/B-ECM@VN group were significantly higher than those in the other groups, and the expression of biomarker Runx2 involved in the development and differentiation of early osteoblasts was the highest on the 7 days, while the marker genes of COL-1, OCN and OPN in middle and late osteoblasts were increased with time. The relative expression level also increased gradually. These results indicated that the $PL_{10}G_1T_1$@N and $PL_{10}G_1T_1$/B-ECM@VN group had the best osteogenic effect.

In situ skull repair experiment was used to further study the osteogenic effect of each scaffold in Sprague-Dawley rat skull defect model, and experimental animals were reviewed and approved by the Experimental Animal Ethics Review Committee of Tongren Hospital. Cylindrical scaffold with a height of 1 mm and a diameter of 5 mm was printed before the operation, which was a good match for the skull defect. All the rats in each group lived well, and none of them were infected or died after scaffold implantation. At 5 and 10 weeks after surgery, Micro-CT scan were performed to observe the regeneration of bone tissue. As shown in Fig. 4A, at 5 weeks of scaffold implantation, the control group had almost no new bone formation without scaffold use, and the four different scaffold groups showed different degrees of new bone tissue. In group $PL_{10}G_1T_1$/B-ECM@VN, the "bone island-like" high density image was observed in the central area of bone defect, and the high density image in the marginal area was dense and regular. At 10 weeks, the healing of bone defect in all groups was significantly increased compared with that at 5 weeks and the degree of new bone formation in group $PL_{10}G_1T_1$/B-ECM@VN was the best at each time point. The results of coronal section are consistent with those of 3D image (Fig. 4A). The quantitative analysis results (Figs. 4B–D) analyzed by CTAn software were consistent with the results of Micro-CT images. The results showed that the rapid release of VIP and continuous release of NGF spatial temporal mode had the most significant influence on bone formation. Finally, according to the survival counts of *Staphylococcus aureus* on the surface of each group of materials, it was proved that the antibacterial sequence designed in this study had high bactericidal activity, and grafting it to the EAKA16 sequence could solve the shortcomings of weak activity and unstable metabolism of natural antimicrobial peptides (Fig. S12 in Supporting information).

In summary, we synthesized a new scaffold, the mechanical properties of the scaffold are close to the strength of human bone, and the degradation rate matches the growth rate of new bone. In addition, compared to the treatment with VIP or NGF, the synergistic effect of these different release kinetics of VIP and NGF showed the highest osteogenic gene expression and mineralization *in vitro* osteogenic studies at the late stage of osteogenic differentiation (days 14 and 21), and the highest bone regeneration *in vivo* animal studies with the highest bone volume/total volume (BV/TV). In addition, B-ECM hydrogel itself has antibacterial activity, and this win-win construction strategy realizes the three basic functions of bone implant including antibacterial, angiogenesis and osteogenesis in one. This work provides insights into the design of advanced functional biomaterials with antimicrobial and bone repair functions.

Declaration of competing interest

The authors declare that they have no known competing financial interests or personal relationships that could have appeared to influence the work reported in this paper.

CRediT authorship contribution statement

Jielin Wang: Writing – review & editing, Writing – original draft, Validation, Supervision, Methodology, Funding acquisition. **Han Ye:** Writing – original draft, Methodology, Data curation. **Bozhuang Zhou:** Methodology, Data curation. **Zhen Pan:** Methodology, Data curation. **Yucai Li:** Methodology, Data curation. **Zhenyuan Wei:** Methodology, Data curation. **Bin Chai:** Software. **Yizhou Gao:** Writing – review & editing, Writing – original draft, Funding acquisition. **Xiaojian Ye:** Writing – review & editing, Writing – original draft, Funding acquisition. **Jiangming Yu:** Writing – review & editing, Writing – original draft, Methodology, Funding acquisition.

Acknowledgments

This work was financially supported by the Laboratory Open Fund of Key Technology and Materials in Minimally Invasive Spine Surgery (No. 2024JZWC-YBA06), Medical and Industrial Cross Research Fundation of "Star of Jiaotong University" Program of Shanghai Jiao Tong University (Nos. YG2022ZD030, YG2021ZD34), Shanghai Jiao Tong University Institute of Minimally Invasive Surgery on Spine (No. 2021JCPT03), Tongren Hospital Introduces the Talented Person Scientific Research Start Funds Subsidization Project (No. TR2022rc07), Tongren Hospital Top Priority Subject Project (No. tr2023xk01), Youth Innovation Promotion Association of CAS (No. 2021264), Shanghai Natural Science Foundation (No. 22ZR1469800).

Supplementary materials

Supplementary material associated with this article can be found, in the online version, at doi:10.1016/j.cclet.2024.110133.

References

[1] D. Nepal, S. Kang, K.M. Adstedt, et al., Nat. Mater. 22 (2023) 18–35.
[2] Z.J. Zou, H. Li, K. Yu, et al., Exploration 3 (2023) 20220132.
[3] Y.T. Wu, X. Zhang, B.W. Tan, et al., Biomater. Adv. 133 (2022) 112641.
[4] S.V. Murphy, P. De Coppi, A. Atala, Nat. Biomed. Eng. 4 (2020) 370–380.
[5] Y. Xu, Y. Li, A. Gao, et al., The Inno. Life 1 (2023) 100015.
[6] X.Y. Wan, Y.C. Zhao, Z. Li, et al., Exploration 2 (2022) 20210029.
[7] K.Q. Huang, J. Huang, J.M. Zhao, et al., Chin. Chem. Lett. 33 (2022) 1941–1945.
[8] X. Qu, M. Wang, M. Wang, et al., Adv. Mater. 34 (2022) 2200096.
[9] Y.J. Li, J.Y. Li, Y.Q. Chang, et al., Chin. Chem. Lett. 35 (2024) 109414.
[10] C. Zhang, A.F. Liu, S.H. Li, et al., Chin. Chem. Lett. 36 (2025) 109752.
[11] M. Xie, Y. Shi, C. Zhang, et al., Nat. Commun. 13 (2022) 3597.
[12] Y. Zhang, D. Li, Y. Liu, et al., Innovation 5 (2023) 100542.
[13] J.L. Wang, J.S. Yu, Y.N. Yan, et al., Polym. Adv. Technol. 30 (2019) 1461–1472.
[14] J.L. Wang, Y.C. Li, Y.Z. Gao, et al., Mater. Today Commun. 31 (2022) 103616.
[15] J.L. Wang, Q. Chen, B.B. Du, et al., Mater. Sci. Eng. C 87 (2018) 60–69.
[16] R.R. Cooper, Science 160 (1968) 327–328.
[17] Q.Q. Wan, W.P. Qin, Y.X. Ma, et al., Adv. Sci. 8 (2021) 2003390.
[18] M. Hayashi, T. Nakashima, M. Taniguchi, et al., Nature 485 (2012) 69–74.
[19] T. Fukuda, S. Takeda, R. Xu, et al., Nature 497 (2013) 490–493.
[20] X. Lv, G. Feng, X. Cao, Cell Metab. 34 (2022) 1914–1931.
[21] E.L. Hohmann, R.P. Elde, J.A. Rysavy, et al., Science 232 (1986) 868–871.
[22] J. Wu, P. Liu, X. Mao, et al., Acta Physiol. 234 (2022) 13767.
[23] M. Casibang, S. Purdom, S. Jakowlew, Lung Cancer 31 (2001) 203–212.
[24] R.E. Tomlinson, Z. Li, Q. Zhang, et al., Cell Rep. 16 (2016) 2723–2735.
[25] A.M. Davies, C. Bandtlow, R. Heumann, et al., Nature 326 (1987) 353–358.
[26] R.E. Tomlinson, Z. Li, Z. Li, et al., Proc. Natl. Acad. Sci. U. S. A. 114 (2017) 3632–3641.
[27] Y.C. Li, Z.Y. Wei, B. Chai, Compos. Part B 275 (2024) 111280.
[28] Z.Y. Wei, H. Ye, Y.C. Li, Acta Biomater. 178 (2024) 50–67.
[29] S.W. Choi, W. Guan, K. Chung, Cell 184 (2021) 4115–4136.
[30] P. Yang, J.H. Zhang, R. Zhang, et al., Green Chem. 26 (2024) 3329.
[31] Y.T. Xu, J.F. Hu, J.J. Hu, et al., Prog. Polym. Sci. 146 (2023) 101740.
[32] P. Yang, W.J. Bai, Y. Zou, et al., Mater. Horiz. 10 (2023) 1020–1029.
[33] H.J. Zhang, Y.Q. Feng, T.Y. Wang, et al., Biomater. Sci. 12 (2024) 2282–2291.
[34] A.P. Dhand, M.D. Davidson, J.H. Galarraga, et al., Adv. Mater. 34 (2022) 2202261.
[35] G. Li, K. Huang, J. Deng, et al., Adv. Mater. 34 (2022) 2200261.
[36] C. Mortier, D.C.S. Costa, M.B. Oliveira, et al., Mater. Today Chem. 26 (2022) 101222.
[37] P. Tan, H. Fu, X. Ma, Nano Today 39 (2021) 101229.
[38] F. Gelain, Z. Luo, S. Zhang, Chem. Rev. 120 (2020) 13434–13460.
[39] K.J. Nagy, M.C. Giano, A. Jin, et al., JACS 133 (2011) 14975–14977.
[40] B. Divband, M. Aghazadeh, Z.H. Al-qaim, et al., Carbohydr. Polym. 273 (2021) 118589.
[41] Z.J. Zhang, F.Q. Wang, X. Huang, et al., Adv. Sci. 10 (2023) 2206155.